International Journal of Rock Mechanics & Mining Sciences 155 (2022) 105138

Contents lists available at ScienceDirect

International Journal of Rock Mechanics and Mining Sciences

journal homepage: www.elsevier.com/locate/ijrmms

# Fractal characteristics of fractures in crystalline basement rocks: Insights from depth-dependent correlation analyses to 5 km depth

Mohammad Javad Afshari Moein [a,*], Keith F. Evans [b], Benoît Valley [c], Kristian Bär [d], Albert Genter [e]

[a] Free University of Berlin, Department of Earth Sciences, Malteserstrasse 74-100, 12249, Berlin, Germany
[b] ETH Zürich, Department of Earth Sciences, Sonneggstrasse 5, 8092, Zurich, Switzerland
[c] University of Neuchâtel, Center for Hydrogeology and Geothermics, Rue Emile-Argand 11, 2000, Neuchâtel, Switzerland
[d] GeoThermal Engineering GmbH, an der RaumFabrik 33c, D-76227, Karlsruhe, Germany
[e] ES-Géothermie, 26, Boulevard du Président Wilson, 67000, Strasbourg, France

ARTICLE INFO

*Keywords:*
Fracture network characterization
Power-law scaling
Spatial distribution
Fractal
Borehole data
Discrete fracture networks

ABSTRACT

The scaling laws describing the spatial arrangement of fractures along six deep boreholes penetrating the crystalline rocks in the Rhine Graben were derived using a correlation analysis. Five of the wells, two to 5 km depth, were located at the Soultz geothermal site and one well to 5 km depth was located at Basel, some 150 km from Soultz. Five datasets were derived from borehole imaging logs, whilst one stemmed from the analysis of 810 m of continuous core at Soultz. The two differed inasmuch as the core dataset included essentially all fractures, whereas the image log dataset had few fractures narrower than 1–3 mm. The results of the analysis for all image datasets showed that the spatial arrangement of fractures followed fractal behavior at all scales from meters to several hundred meters, the largest scale amenable to assessment, and that the fractal dimensions were confined to the narrow range 0.85–0.9. However, the core dataset showed significant deviation from fractal behavior, the best-fit fractal dimension of 0.8 being somewhat lower than values obtained from imaging logs in neighboring wells. Eliminating fractures with apertures less than 1 mm from the core dataset to improve comparability led to even lower fractal dimension estimates, indicating the discrepancy was not due to imaging log resolution. Analysis of successive depth sections of the core log suggested the discrepancy was due to the presence of a localized zone between 1750 and 2070 m where the fractal organization is disturbed or takes a lower dimension than elsewhere. Aside from this zone, no systematic variation of fractal dimension with depth was observed in any dataset, implying that a single exponent together with intensity adequately describes the arrangement of fractures along the entire length of the boreholes. The results are relevant to the parameterization of DFN models of deep rock masses.

## 1. Introduction

Fractured rock masses play host to many underground engineering activities such as conventional and unconventional hydrocarbon recovery, radioactive waste disposal, underground gas/$CO_2$ storage and geothermal energy exploitation.[1–5] The fracture network controls not only the fluid flow and transport patterns[6–8] but also in-situ stress, or rock deformation,[9–12] heat transport (e.g. Refs. 13–18 and the induced seismicity.[19–22] Most underground engineering activities benefit from knowledge of the characteristics of the fracture network, with some requiring the development of a discrete fracture network model (DFN) for the rock mass in question. A case in point is the development of Engineered Geothermal Systems (also known as Enhanced Geothermal Systems, hereafter EGS) in deep, low-porosity rocks. In essence, such systems require the engineering of a heat exchanger within the natural fracture system that links two or more boreholes, often at considerable depths. Fluid can then be circulated around the loop and heat extracted at the surface. To support commercial flow rates, it is usually necessary to enhance the permeability and inter-linkage of the rock mass fractures. This is most commonly accomplished by hydraulic stimulation, whereby the formation pressure within the reservoir is raised by conducting high-volume, high-rate injections into the boreholes so that the fractures

* Corresponding author.
*E-mail address:* mohammad.moein@geophysik.fu-berlin.de (M.J. Afshari Moein).

https://doi.org/10.1016/j.ijrmms.2022.105138
Received 11 April 2021; Received in revised form 9 April 2022; Accepted 13 May 2022
Available online 27 May 2022

are weakened and fail in shear, resulting in irreversible dilation (e.g. Refs. 23,24. Classic Mode 1 fractures may also develop, particularly near the injection wells. The processes are complex and involve a hydro-thermo-mechanical interplay between the stress field, the fractures, and the intact rock (e.g. Ref. 25. Numerical reservoir models which simulate these processes and include realistic descriptions of the fracture network and stress state are a key tool for evaluating a reservoir's economic potential and optimizing the design of the stimulation. Thus a 3-D representation of the fracture network within the target rock mass is essential. Typically, the fracture networks that feature in such models are realizations that are generated stochastically from statistical parameters extracted from line-samples of the fractures intersected by boreholes, which usually are the only direct source of information about the fracture network in the target rock mass. The realizations may also include deterministic information on the location of major fracture zones from the boreholes and other sources, including hydraulic data,[26–28] in situ stress[29,30] and patterns of induced seismicity.[31,32]

Various statistical techniques have been applied to 1D fracture datasets from scanlines or boreholes in order to characterize attributes of the fracture network.[33–36] Among them, the power-law scaling that underlies fractal theory has been found to well describe various geometrical attributes of the fractures such as length and spatial distribution,[37–39] although little information on the fracture length distribution can be extracted from 1D datasets. The simplest statistical approach is to examine the frequency distribution of fracture spacing along the borehole. If the distribution is fractal, then it would be a straight line in log-log space. However, this approach has been found to be unstable, even when applied to synthetic fractal datasets.[40] A weakness of the method is that it considers only the spacing of neighboring fractures, and disregards the sequence of spacing.[41] Another approach to derive scaling laws is by the analyses of 1D fracture patterns using the box-counting technique, which is also known as Cantor's Dust method.[42–44] For instance, Ref. 45 applied this method to one of the datasets examined in the present study and found that fractal dimension tended to increase with depth, a result they proposed was due to the increase of lithostatic pressure gradient in the earth. Although the box-counting technique is widely applied in literature, it is now well recognized that the fractal dimension estimates derived from the method are prone to the influence by finite size effects.[37,40] Hence, it is clearly relevant to examine whether the increase of fractal dimension with depth holds when a more robust method is implemented.

The two-point correlation function or correlation integral method,[46] which is the method we use in this paper, considers the sequence of fractures, and has been found to give greater stability.[40] Specifically, we analyzed the spatial arrangement of fractures identified along six sub-vertical, deep boreholes in crystalline rock of the Rhine Graben in Central Europe using the normalized correlation integral (NCI) method. Five of the wells, GPK1, GPK2, GPK3, GPK4, and EPS1, were located at the Soultz EGS site and one well was located at Basel, some 150 km to the south of Soultz. The datasets from GPK3, GPK4 and BS-1 extend to 5 km depth. In all but one case the data are derived from imaging logs run in the wells, the exception being the data from well EPS1 at Soultz which stem from visual inspection of 810 m of continuous core down to 2227 m depth. In a previous paper,[40] the data from GPK3, GPK4 and BS-1 were analyzed using the unnormalized correlation integral method, and it was shown that the arrangement of fractures in all three wells followed a fractal scaling law with a fractal dimension of 0.86–0.88. It was also shown that the members of the fracture sets (defined in terms of orientation) at the two sites also followed a fractal arrangement in the wells, albeit with a lower fractal dimension of 0.65–0.75. In this paper, we build upon the previous work and make as more detailed comparison of the scaling laws using data from more wells to assess the consistency of the scaling between wells at the same site, and also examine the possibility that scaling changes with depth. In contrast to the previous paper, we evaluate scaling using the normalized form of the correlation integral to give greater comparability in the results from datasets of different length. In summary, the objects of this paper are: 1) Apply the correlation integral method to analyze the arrangement of fractures in all six wells and determine whether it conforms to power-law scaling, and if so, determine the fractal dimension and range of length scales over which it applies; 2) Compare the fracture scaling characteristics obtained in the five wells at the Soultz site; 3) Compare the scaling characteristics obtained from the core log at Soultz with those from image logs run in neighboring wells, 4) Perform scaling analyses on sub-intervals along the datasets to examine the stationarity of scaling laws with depth. The results should be of interest to any underground engineering application where fracture network characterization is important, and the primary source of information on the fracture network is from boreholes.

## 2. Study sites and 1D natural fracture datasets

The 1D fracture datasets were obtained in six deep boreholes drilled into crystalline rocks in the URG, which is a Cenozoic rift system.[47] Five wells were located at the Soultz-sous-Forêts EGS site in France, and one well, BS-1, was located at the Basel geothermal project, Switzerland. The geological setting of the URG is presented in Fig. 1. The URG extends over 300 km from the city of Frankfurt in Germany in the North to the city of Basel in Switzerland in the South. In total, five image log datasets and one core dataset were analyzed. The datasets used in the study are summarized in Table 1. All the six datasets include true vertical depth (TVD), and true dip and dip direction of the fractures corrected for borehole inclination. The image log datasets derive largely from acoustic

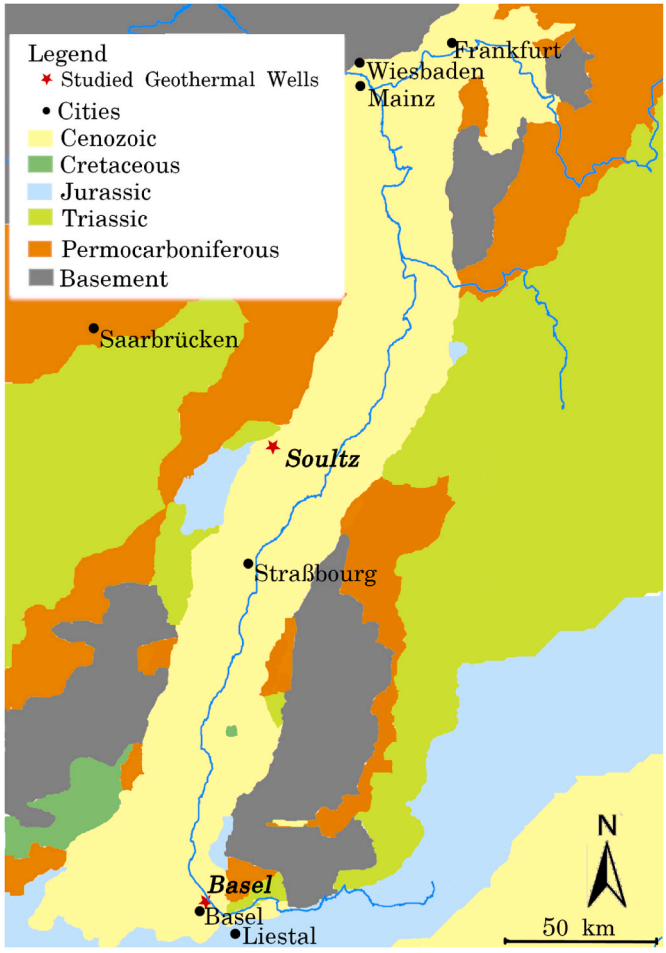


**Fig. 1.** Overview of the geological setting of the Upper Rhine Graben in Europe, where Soultz-sous-Forêts and Basel EGS projects (the study sites) are located (Geology after.[49])

**Table 1**
Summary of source information for all 1D fracture datasets from boreholes within the crystalline basement of the Upper Rhine Graben.

| Well | Site | Depth Interval [m] | Source | Fracture Count | Reference |
|---|---|---|---|---|---|
| BS-1 | Basel | 2600–5000 m | UBI | 1164 | [50] |
| GPK1 | Soultz | 1960–3600 m | FMI | 593 | [51] |
| GPK2 | Soultz | 1420–3800 m | UBI | 1785 | [52] |
| GPK3 | Soultz | 1420–5000 m | UBI | 1926 | [36] |
| GPK4 | Soultz | 1420–5000 m | UBI | 2115 | [36] |
| EPS1 | Soultz | 1417–2227 m | Cores | 2997 | [53] |

televiewer logs (UBI), the exception being that for GPK1 which was from an FMI log. The core dataset was from well EPS1 at the Soultz site stemmed from a detailed analysis of 810 m of continuous core to 2227 m.[48]

The core dataset differs fundamentally from those from the image logs inasmuch as it presents a relatively complete and accurate description of fractures along the borehole, and included width information. Some 75% of the fractures identified had width less than 1 mm.[52] compared the core dataset to that obtained from an acoustic televiewer log run in the same well,[54] and found that in crystalline rock, the televiewer had difficulties resolving fractures with a width less than 1 mm, or those that lay within 5 mm of a neighbor. The detectability of fractures in acoustic televiewer logs depends upon the frequency of the tool, the diameter of the borehole, logging speed, rock properties, and the type and degree of alteration of the fracture amongst other things. Thus, it is difficult to make simple statements about the minimum aperture that is detectable by the logs that feature in this study, although it is probably of the order of 1–3 mm.[52,55] In this study, we will consider that the EPS1 core dataset provides a complete detectability of the fractures intersected by the borehole, and as such serves to provide ground truth.

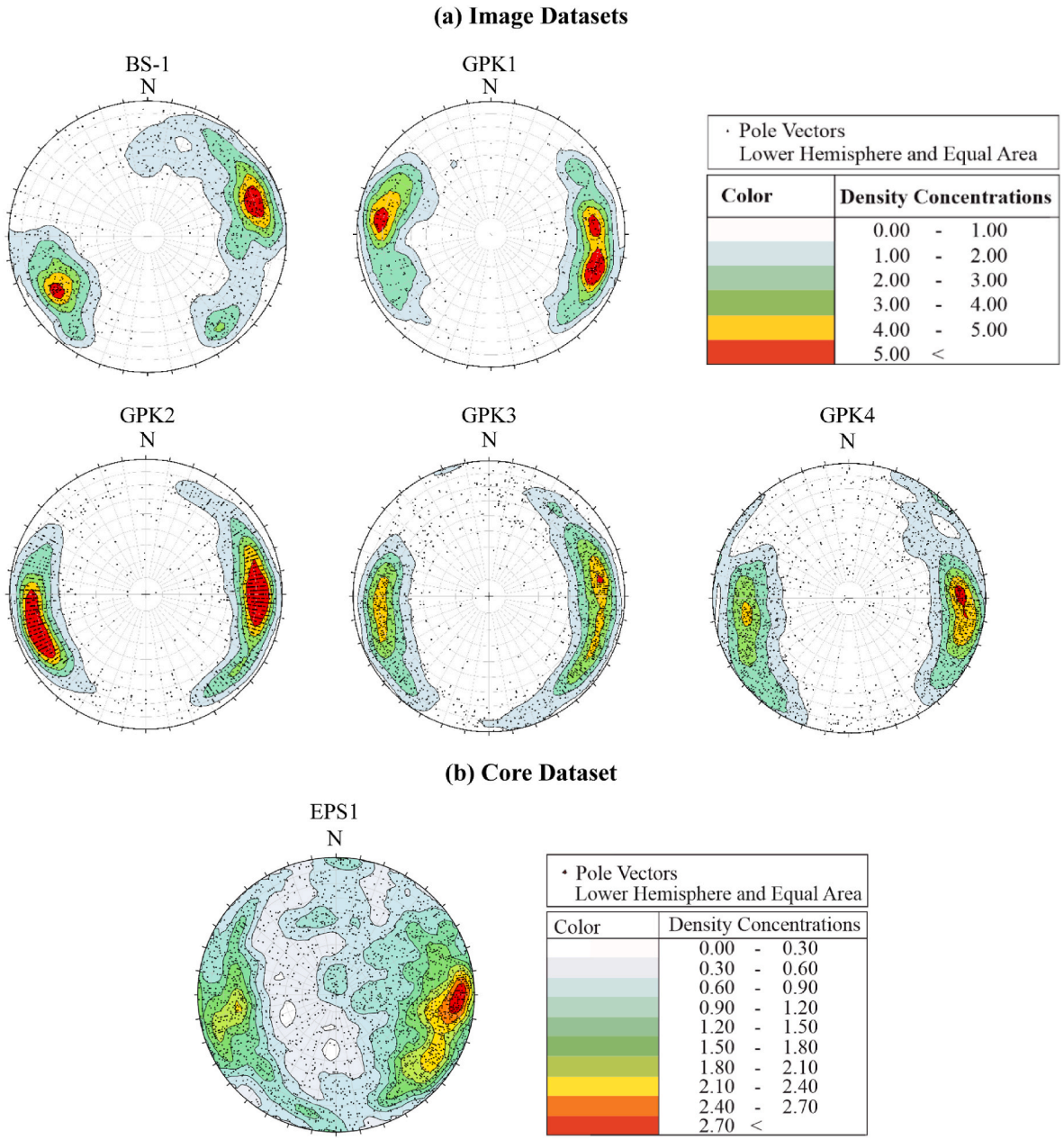


**Fig. 2.** Equal area, lower hemisphere stereographic projections of pole vectors to all fractures identified in (a) borehole image logs from the BS-1, GPK1, GPK2, GPK3 and GPK4 (b) cores from EPS1 wells. Contours display the pole point densities using a Fischer distribution with a counting circle size of 1%. The contours' range vary between 0 and 6 fracture density concentrations in six ten equispaced intervals in (a) and between 0 and 3 in ten equispaced intervals in (b).

### 2.1. Basel geothermal project

#### 2.1.1. BS-1

In 2006, the BS-1 well was drilled into a depth of 5 km beneath the city of Basel with the aim of developing an EGS. Basel is located in northwestern Switzerland in the Upper Rhine Graben close to the northern thrust of Jura Mountains (Fig. 1). The well penetrates 2.4 km of Quaternary, Tertiary, and secondary sediments, 100 m of red Permian siltstone and weathered granite, and 2.5 km of crystalline rocks that are exclusively plutonic rocks with no observed metamorphism.[56] The crystalline rock types include mainly granitoid rocks (>99%) cross-cut by aplitic and lamprophyric dykes consisting of quartz, K-feldspar, plagioclase, biotite, hornblende and titanite [57]. The uppermost 400 m of the basement is highly altered and fractured, since it was exposed at the surface prior the deposition of the Permian sedimentary succession. BS-1 is approximately vertical and was imaged from 2.557 km to 5 km using an Ultrasonic Borehole Imager (UBI) with a vertical resolution of approximately 1 cm.[58] Fig. S1 (supplements) depicts a vertical cross-section showing the borehole trajectory.[50] examined the image logs from the crystalline basement between 2.6 and 5 km and identified 1164 natural fractures. The poles to these fractures are shown in the lower-hemisphere, equal area stereographic projection in Fig. 2.

### 2.2. Soultz-sous-Forêts geothermal project

The Soultz-sous-Forêts geothermal site, also known as European EGS project, is located at the western edge of the Upper Rhine Graben in France (see Fig. 1). Since the start of the project in 1987, five boreholes were drilled or extended to develop a heat exchanger within the basement rocks that lie under 1.4 km of Cenozoic and Mesozoic sedimentary cover. Two exploratory wells, EPS1 and GPK1, and three exploitation wells, GPK2, GPK3 and GPK4, were drilled to investigate the scientific questions relevant to developing EGS technology.[59] Fig. S2 depicts a vertical cross-section showing the borehole trajectories and the lithological units. The datasets used in this study consist of image logs for four boreholes and continuous coring for the remaining hole (EPS1). The fracture image logs were derived from either ultrasonic televiewer or microresistivity sondes.

#### 2.2.1. GPK1, GPK2, GPK3, GPK4 and EPS1 wells

The basement in the Soultz area is mainly composed of late Hercynian monzogranites containing phenocrystals of alkali feldspars in a matrix of quartz, biotite, plagioclase and few amphibole.[60,61] The monzogranite extends from the sediment interface at 1420 m–4700 m depth, and displays a weak pervasive alteration and marked hydrothermal vein alteration that is intense between 2800 and 3400 m. Below 4700 m, a fine-grained two-mica granite is found.[62] There is no aplitic neither lamprophyric dykes in the Soultz basement.

The GPK1 exploration well was drilled to 2000 m in 1987 and then extended to 3600 m in 1992. The fracture dataset for this well were acquired using microresistivity sondes and the interpretation of FMI (Formation Micro-Imager) logs run between 1960 and 3600 m depth and consists of 593 natural fractures.[63] Wells GPK2, GPK3 and GPK4 were all drilled to 5 km depth from the same pad. GPK3 and 4 were both deviated towards the south below about 2.3 km, so that the open-hole sections of the three wells form an approximately in-line triplet with GPK3 at the center and a ~700 m well spacing (Fig. S2). GPK2 was initially drilled to 3880 m in 1999 and was logged with UBI acoustic televiewer.[52] analyzed the log and identified 1785 natural fractures between 1420 and 3880 m. The well was then deepened to 5000 m in 1999 and 1 m of core taken from near the bottom. A UBI and an Azimuthal Resistivity Imager (ARI) log were also attempted. The ARI log yielded interpretable images between 3880 and 5093 m, but the azimuthal resolution was too poor for the log to be used in the present analysis. Wells GPK3 and GPK4 were destructively drilled in 2003 and 2004 respectively and UBI logs successfully run in both wells.[36] analyzed both logs between 1400 and 5000 m and generated datasets containing 1926 and 2115 fractures in GPK3 and GPK4 respectively (Table 1).

Borehole EPS1 was drilled to a depth of 2227 m, and was cored below 1417 m resulting in 810 m continuous core in the crystalline basement.[53] The core sections were oriented by comparing common features seen in both core and an ultrasonic televiewer log[54].[48] analyzed the fractures from core samples and identified the depth, orientation, type, aperture and information on the mineral infill of 2997 fractures. Unfortunately, the fracture dataset derived from the televiewer by[54] appeared to include both induced and natural fractures.[52] For instance, the core log showed very few fractures in the depth range 1920–2050 m, whereas the image log indicated a fracture frequency of 0.6 fractures/meter (see Fig. S3 in the supplementary material). Hence, this dataset was excluded from the present analysis. Stereographic projections of the poles to fractures along the GPK1-4 and EPS1 wells are shown in Fig. 2. The fracture densities of all the available datasets are plotted against the corresponding depth in Fig. S4.

## 3. Methodology

Fractal geometry has been widely used to characterize many geological phenomena such as fracture and fault networks (e.g. Refs. 39,[64], earthquake hypocenters (e.g. Refs. [65–69], elastic heterogeneity[70,71] and in-situ stress variability (e.g. Ref. [72]. In the case of 1D fracture datasets, various methodologies were applied to derive the scaling laws of spatial distribution. These include box-counting technique,[73] correlation integral[41,74–76] and power-law fitting to spacing data.[42] Among them, correlation integral computes the probability of finding a pair of fractures that have a given center-to-center distance.[46] The NCI characterizes the spatial distribution of fracture patterns in 1D, 2D and 3D fracture datasets by the following equation:

$$C_2\left(r/L\right) = \frac{2N_p\left(r/L\right)}{N_t[N_t-1]} = \Lambda\left[r\Big/L\right]^{D_2} \tag{1}$$

where $N_t$ is the total number of fractures, $N_t[N_t-1]/2$ is the total number of pairs of fractures, $N_p\left(r/L\right)$ is the number of pairs of fractures whose center-to-center normalized distance is less than $r/L$ in a domain (line, square or cube) of size $L$, $D_2$ is the correlation dimension, and $\Lambda$ is a constant.[74] The normalization of the correlation integral enables a direct comparison of 1D datasets to be made that is independent of the system size (i.e. various interval lengths, Table 1). We also adopted the hypothesis that the fracture systems in geological systems is monofractal,[37] so that a single exponent (such as correlation dimension) is sufficient to define the multifractal spectrum. Hence, correlation dimension and fractal dimension can be used interchangeably.

For fractally-distributed datasets, the local slope of the NCI in a log-log space is linear, indicating a power-law scaling relation. The slope gives the correlation dimension, $D_2$, which is equivalent to the fractal dimension. In practice, the NCI deviates from linearity at scales larger than $0.1L$ (i.e. $\frac{r}{L} > 0.1$) due to boundary effects, and at scales smaller than ~0.001 due to progressive undersampling of the fracture population arising from the failure to resolve closely-spaced fractures, particularly in fracture zones. As shown in Table 2, for the datasets analyzed, the normalized limit of 0.001 is equivalent to length scales of 1–3 m, which probably overestimates the scale at which undersampling becomes significant. These constraints on power-law scaling are intrinsic limitations of the applied methodology. Thus, the fractal scaling parameters $D_2$ and $\Lambda$ were computed by fitting a line to NCI over the normalized scale range, $r/L$, of 0.001–0.1. The standard error in the $D_2$ estimate reflects the degree to which the scaling is fractal over this range. The error bars are the standard deviation of the fit of a linear trend to the normalized correlation integral over the normalized range. Deviations are best identified by plotting the slope function, which is the

**Table 2**
Summary of fractal analyses of six 1D fracture datasets. The range of power law is simply the unnormalized equivalent range of the normalized range 0.001–0.1.

| Well | Dataset length [m] | Average density [$m^{-1}$] | $D_2$ | $\Lambda$ | Power-law scale [m] |
|---|---|---|---|---|---|
| BS-1 | 2600 | 0.49 | $0.85 \pm 0.04$ | $2.3 \pm 0.07$ | 2–239 |
| GPK1 | 2224 | 0.27 | $0.89 \pm 0.04$ | $1.61 \pm 0.06$ | 2–160 |
| GPK2 | 2380 | 0.75 | $0.90 \pm 0.03$ | $1.80 \pm 0.06$ | 2–236 |
| GPK3 | 3580 | 0.53 | $0.88 \pm 0.02$ | $1.49 \pm 0.04$ | 4–359 |
| GPK4 | 3580 | 0.59 | $0.88 \pm 0.05$ | $1.52 \pm 0.09$ | 4–352 |
| EPS1-Cores | 810 | 3.7 | $0.8 \pm 0.09$ | $1.58 \pm 0.1$ | 1–81 |

local slope of the NCI in log-log space, given by:

$$\text{Local Slope} = d\left\{\log\left[C_2\left(r/L\right)\right]\right\}\Big/ d\left\{r/L\right\} \quad (2)$$

The parameter $\Lambda$, referred to as the power-law scaling coefficient, quantifies the offset of the power-law fit to NCI, and corresponds to the intersection of the fitted line with the vertical line at $r/L = 10^0$ in log-log space. The errors of the $\Lambda$ estimates were computed as the difference between maximum and minimum offsets of the linear fits for all possible $D_2$ values within the standard error.

## 4. Results

### 4.1. Comparative correlation analyses of fractures in the wells

We began the analysis by computing the NCIs of fractures at five image log datasets: BS-1 and GPK1/2/3/4. NCIs were computed for 100 logarithmically distributed normalized distance of 0.0001–1.0, delivering 25 values per decade. The local slopes and scaling coefficients were computed by linear fit to the NCIs over windows of five neighboring points without any overlap. Therefore, five pairs of local slopes and scaling coefficients were computed for every decade. The reported values of $D_2$ and $\Lambda$ were the mean values of the slopes and coefficients within the normalized range of 0.001–0.1. The error estimates of $D_2$ were the standard deviation of those 15 values of local slope. Moreover, the errors of the $\Lambda$ estimates were computed as half the difference between maximum and minimum offsets of the linear fits for all 15 local slopes. The NCIs and slope-functions obtained for each well are shown on Fig. 3 together with the best-fitting line over the range, 0.001–0.1, and the implied scaling parameters, $D_2$ and $\Lambda$ whose values are also listed in Table 2. Also shown are expected slope functions for fractally-distributed fracture profiles of identical length, number of fractures, and $D_2$ values obtained from the linear fits. Each is an average of 100 slope functions produced from 100 fracture distributions generated using a Multiplicative Cascade Process MCP.[77] The MCP is widely used to generate monofractal fracture centers with any correlation dimension between 0 and 1 that are comparable to 1D datasets from boreholes. A detailed step-by-step methodology to generate synthetic fracture patterns in 1D, 2D and 3D using MCP was presented by[40] and the same methodology was implemented, here. In all cases, the expected slope functions are reasonably flat at the level of the input $D_2$ value over the range 0.001–0.1. These provide the reference against which the degree to which the slope function derived from the dataset in question conforms to fractal behavior over the range 0.001–0.1 can be judged. It is evident that although the five datasets in Fig. 3 spanned different interval lengths (see Table 1), all correlation integrals showed scale-invariance over at least two orders of magnitude of scale, the associated correlation dimensions lying between 0.85 and 0.90 with errors of 0.05 or less. The corresponding $\Lambda$ values lay between 1.49 and 2.3.

The procedure used to analyze the fracture distribution from the EPS1 core dataset was identical to that used for the image logs. The results are shown on Fig. 4a and listed in Table 2. The best-fit linear trend to the NCI between 0.001 and 0.1 yields a slope equivalent to a correlation dimension of 0.8, although the deviation of the slope function from that expected for this correlation dimension is relatively large, as quantified by the standard error of ±0.09. Since the image log dataset from the EPS1 well is excluded from the analyses, a direct comparison of image logs and cores was not feasible. To generate a dataset that is comparable to image logs, fractures with an aperture less than 1 mm were excluded from the core dataset, and the NCI analysis were repeated. As stated earlier, the minimum width of fractures required for detection by the image logs is estimated to be 1–3 mm. To make the EPS1 log more comparable with the image logs, we experimented by excluding fractures with an aperture less than 3 mm from the EPS1 dataset, but found that there remained only 184 fractures, which was not sufficient for a robust correlation analysis (see Section 4.4). Therefore, we adopted a threshold of 1 mm that gave 738 fractures, which was sufficient for the NCI analysis. The normalized correlation integral (NCI) and slope functions are plotted in Fig. 4b and reported in Table 2. The correlation dimension was $0.71 \pm 0.09$, which is lower than that of the entire dataset. This result will be further examined in Section 4.5.1.

### 4.2. Impact of fracture counts on the scaling laws in 1D natural fracture datasets

The six datasets analyzed had different fracture counts and spanned over different interval lengths. Since the correlation analyses were performed using normalized distances, different interval lengths should not affect the scaling laws. Here, we further examined the impact of fracture counts on the scaling laws of natural fracture datasets. Fig. 5 plots the $D_2$ and $\Lambda$ values of six natural fracture datasets against the number of fractures they each contain. The correlation dimension estimates of the five image-log datasets scatter close together, regardless of the diverse fracture counts, whereas the estimate for the EPS1 core-derived dataset, which contains substantially more fractures and has a higher fracture density (Table 2), is lower that of other datasets. The corresponding $\Lambda$ values did not show a systematic dependence on the number of fractures in each dataset.

### 4.3. Parameters controlling the scaling laws

For a distribution of fractures that obeys fractal scaling, the fractal dimension is a number between 0 and 1 with lower values indicating a higher degree of clustering. A fractal dimension is 1 or very close to 1 indicates the spatial distribution can be simulated by Poisson process. The fractal dimensions of spatial distribution in five image log datasets, as given by the correlation dimensions, revealed relatively similar values in the range 0.85–0.9. However, a broader range of values was found for the power-law scaling coefficient $\Lambda$, which reflects the offset of the linear fits to the correlation functions of different datasets.[35] suggest this offset is related to fracture intensity, which is equivalent to density for 1D datasets. To evaluate this hypothesis, we assessed the impact of fracture density on $\Lambda$ values by analyzing synthetically-generated 1D fracture patterns. We applied the 1D MCP fractal generator so as to secure the full control over the correlation dimension and the number of fractures.

We began by generating 1D fracture patterns with a correlation dimension, $D_2$, of 0.75 in a domain size of $L = 1000$ m. A range of fracture counts were chosen (i.e. 250, 500, 1500, 2000, 2500, 3000,

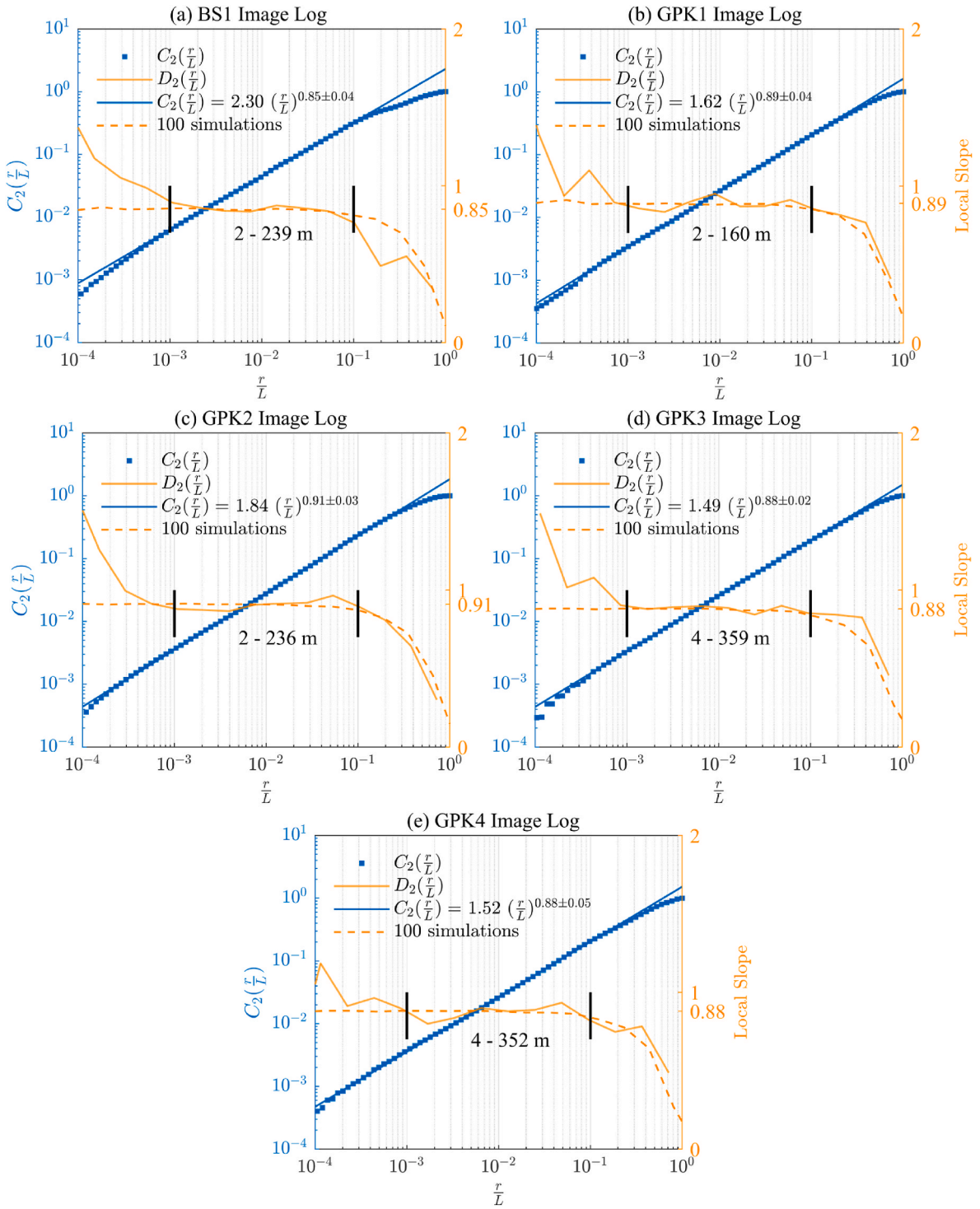


**Fig. 3.** Normalized correlation integrals ($C_2(r/L)$ - blue squares) and corresponding local slope functions (orange solid lines) of fractures derived from all dataset. The approximately linear trends of the NCIs denote fractal scaling, the slopes indicating the correlation dimensions $D_2$. The parameters in the scaling relationships shown in the Figure and listed in Table 2 were computed by fitting a line in log-log space to the NCIs over the normalized range 0.001–0.1. The standard error in the slope of this fit reflects the degree to which the scaling is fractal over this range. The range of fractal scaling can be seen by comparing the slope functions (blue solid lines) with the dashed lines, which represent the expected slope functions for profiles of identical length and number of fractally distributed fractures with $D_2$ values obtained from the linear fits. The expected slope functions represent the average of 100 distributions generated using the MCP. (For interpretation of the references to colour in this figure legend, the reader is referred to the Web version of this article.)

3500 and 4000) that cover all likely natural fracture densities observed in 1D datasets (average densities between 0.27 and 3.7, Table 2 column 3). For each fracture count (e.g. 250 fractures), 50 random realizations with the same number of fractures (e.g. 250) were generated. For each realization, the NCI analysis was performed and the values of $\Lambda$ computed. Fig. 6 plots the box-chart of $\Lambda$ estimates as a function of fracture density. This figure shows that various realizations with the same $D_2$ and density may have different $\Lambda$ estimates and the power-law

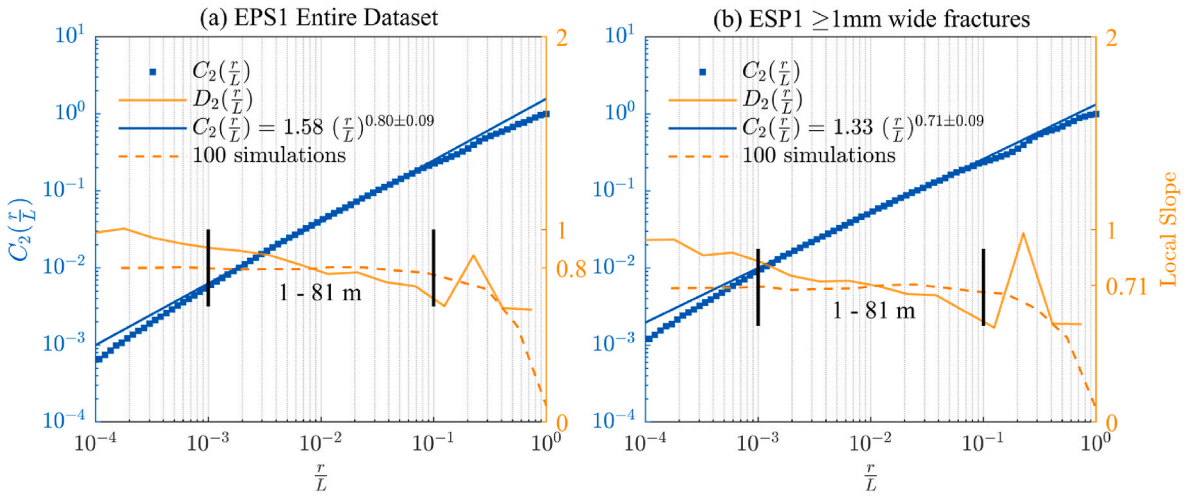


**Fig. 4.** Normalized correlation integrals and local slope functions of fractures derived from cores at EPS1 well. (a) NCI analyses of the entire fracture datasets and (b) displays the same analyses for the dataset containing only fractures with a width ≥1 mm. The mean slopes given in the scaling law equations are computed from the slope functions over the ranges indicated by the bold vertical lines and are indicated by the thin horizontal lines.

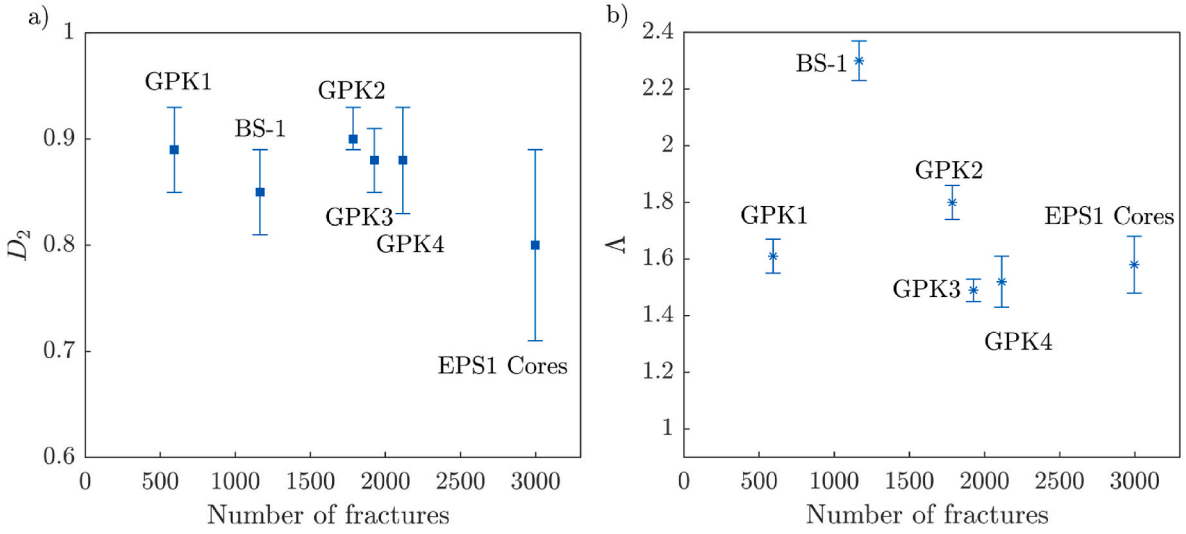


**Fig. 5.** a) Correlation dimension estimates and b) $\Lambda$ values of seven 1D datasets versus the number of fractures. All the datasets were derived from image logs except EPS1 cores.

scaling coefficient is not directly controlled by the fracture density.

### 4.4. Impact of fracture counts on the precise derivation of $D_2$

The parameters of the scaling laws listed in Table 1 were derived for the entire depth intervals of natural fracture datasets. To resolve any possible depth-dependence of clustering would require the analysis be conducted on successive, shorter depth intervals which would necessarily contain fewer fractures that the entire interval. Thus, before proceeding, it is relevant to assess the smallest number of fractures in an interval needed to yield a robust estimate of $D_2$.[34] proposed that 300 data points is sufficient to characterize the spatial distribution that span over three orders of magnitude. To assess whether this holds for the estimation of correlation dimension, we utilized synthetic fractal patterns to assess the impact of the number of fractures on the uncertainty in the estimation of the $D_2$. We began by generating a 1D fracture network of 10000 fractures with a correlation dimension of $D_2 = 0.75$ (close to lowest correlation dimension of 1D natural fracture datasets), in a domain size of $L = 1000$ m. Since we used the normalized form of the correlation integral (NCI), the domain interval length did not affect the analyses. The 10000 fractures in the 1000 m domain size yielded a mean fracture density of 10 fractures/m, which is higher than the value of 3.7 found for the density of fractures at EPS1 core dataset. Fig. 7a displays a short 100 m interval of the synthetic 1D dataset.

To begin the sensitivity analysis, a series of fracture counts were chosen (i.e. 200, 500, 1000, 2000, 3000, …8000). For each fracture count (e.g. 200 fractures), 100 random realizations with the same number of fractures (e.g. 200) were randomly selected from the initial dataset. For each realization, the NCI was computed using the methodology described in section 3 (i.e. $C_2(r/L)$ was computed for 100 logarithmically-spaced points per decade for $r/L$ values between 0.0001 and 1.0). The slope function was then determined by averaging point-to-point slopes within successive 20-point windows. The $D_2$ value was then computed by taking the average value of the slope function over the $r/L$ range 0.001–0.1. Visual inspection confirmed that all computed slope functions generated in the study were reasonably flat within this range at least (similar to natural fracture datasets). The resulting values of $D_2$ were plotted as a function of the number of fractures for 100 realizations in Fig. 7b. Evidently, the scatter in the values decreased at the number of fractures in the window increased. According to Fig. 7b, reasonably

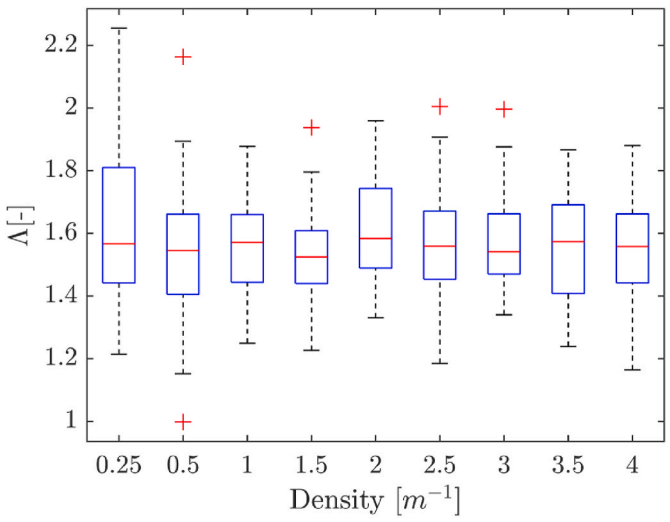


**Fig. 6.** (a) Box-plots of $\Lambda$ estimates for 50 random realizations with the same density. All the realizations were generated over a length of $L = 1000$ m with a fractal dimension of 0.75. For a given density, the red line in the boxes denotes the median of $\Lambda$ while the 25 and 75 percentile values are presented by the box itself, with a difference of interquartile range (IQR). The short black lines are 1.5 times IQRs away from 25 to 75 percentiles. The red crosses are the outliers. (For interpretation of the references to colour in this figure legend, the reader is referred to the Web version of this article.)

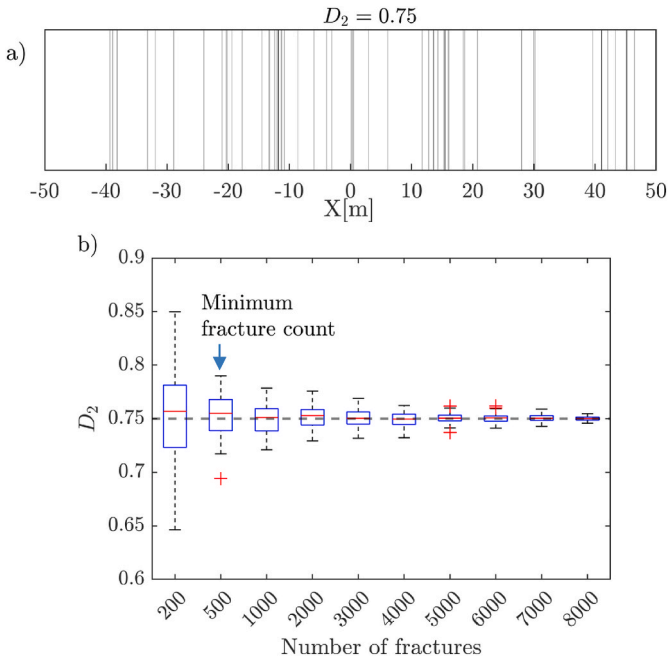


**Fig. 7.** (a) A schematic view of a synthetic 1D fractal fracture network using Multiplicative Cascade in a domain length of $L = 1000$ and 10,000 fractures in the entire domain. For the sake of clarity, only 100 m of the interval is displayed. (b) Box-plots of $D_2$ estimates of 100 realizations for each fracture count. For a given number of fractures, the red line in the boxes denote the median of $D_2$ while the 25 and 75 percentile values are presented by the box itself, with a difference of interquartile range (IQR). The short black lines are 1.5 times IQRs away from 25 to 75 percentiles. The red crosses are the outliers. The corresponding plot of $\Lambda$ values is presented as Fig. S5 of the supplementary material. (For interpretation of the references to colour in this figure legend, the reader is referred to the Web version of this article.)

stable estimates were obtained for 500 or more fractures and the deviations from the true $D_2$ were less than the errors of natural fracture datasets (Table 2, column 4). This gave an approximate window size over which the $D_2$ estimates were scattered in a reasonably narrow range. However, one cannot exclude the possibility of a choosing a realization with a much higher or lower $D_2$ estimate, similar to the outliers in Fig. 7b. Thus, we adopted the 500 data points as the minimum window size needed to ensure reliable estimation of $D_2$ in the 1D line sampling. This window size was applied to perform a depth-dependent clustering analysis in the following section. Fig. S5 also plots the values of $\Lambda$ associated with the synthetic series of Fig. 7a. The $\Lambda$ values ranged between 0.5 and 2.5, which were very similar to the values found for the natural fracture datasets.

### 4.5. Depth-dependent correlation of 1D natural fracture datasets

According to the previous section, analyzing the depth-dependent clustering of fractures requires that the borehole dataset in question contains sufficient numbers of natural fracture. Since the GPK1 dataset did not meet this requirement, it was excluded from the depth-dependent analyses.

#### 4.5.1. EPS1 core dataset

The EPS1 core dataset was evaluated by computing the NCI in moving windows containing 1000 and 500 fractures. The analysis for 1000-fracture intervals was expected to yield smaller errors on the $D_2$ estimates, but at the expense of requiring larger and hence fewer depth intervals. For both windows sizes, a 50% overlap was used to maximize the number of $D_2$ determinations. The procedure used to estimate the $D_2$ and $\Lambda$ values and their standard deviation for each window was identical to that described in Section 4.4. Fig. 8a shows the $D_2$ and $\Lambda$ value estimates for the 1000-fracture intervals. The spread of the intervals that define each datapoint is shown below in Fig. 8b and individual NCI analyses of five windows with 1000 fractures are also plotted in Fig. S6. The corresponding plots for the 500-fracture intervals are shown in Fig. 8c–d. It is clear that the errors for the $D_2$ estimates is much larger for the 500-fracture intervals than those for the 1000-fracture intervals. The profile of fracture density as defined in a 1 m moving window is plotted in Fig. 8e together with cumulative fracture count. Evidently, density varies from zero up to 32 fractures/m for the densest clusters. It is noteworthy that there is a near-absence of fractures between 1920 and 2050 m, a 130 m hiatus that is not seen in any other well at the Soultz site. Neither the 500- nor 1000-fracture profiles show a systematic depth dependence of $D_2$ and $\Lambda$ over the 800 m core interval. However, both profiles suggest a slight drop in the $D_2$ estimates in the depth range 1750–2000 m. Whilst the errors are large, the drop in $D_2$ value around 1900 m depth is statistically significant in both cases, at least when compared with the values above 1550 m. The corresponding estimates of $\Lambda$ also show significant variation with depth, the values ranging between 0.96 and 4.3, although the variations for the 500- and the 1000-fracture windows are not the same. These results will be addressed later in Section 5.

#### 4.5.2. BS-1, GPK2, GPK3 and GPK4 image log datasets

The profiles of $D_2$ and $\Lambda$ for the BS-1 dataset were computed in stepped windows of 500 fractures with overlaps of 250 fractures, and the results are shown in Fig. 9a. No significant variation with depth is evident for either parameter. The average $D_2$ values ranged between 0.84 and 0.9 and the $\Lambda$ values lay between 1.45 and 1.86. A notable feature of this dataset is the presence of a paleo-weathered surface in the uppermost 400 m of the granite (2600–3080 m), which is evident in the fracture density and cumulative fracture count profiles shown in Fig. 9b. This zone accounts for almost 50% of the total fracture count in the well, and has fracture densities of up to 10 fractures/m.

Similar depth-dependent analyses were performed for the three datasets of GPK2/3/4. Figs. 10 and 11 display the fractal dimension

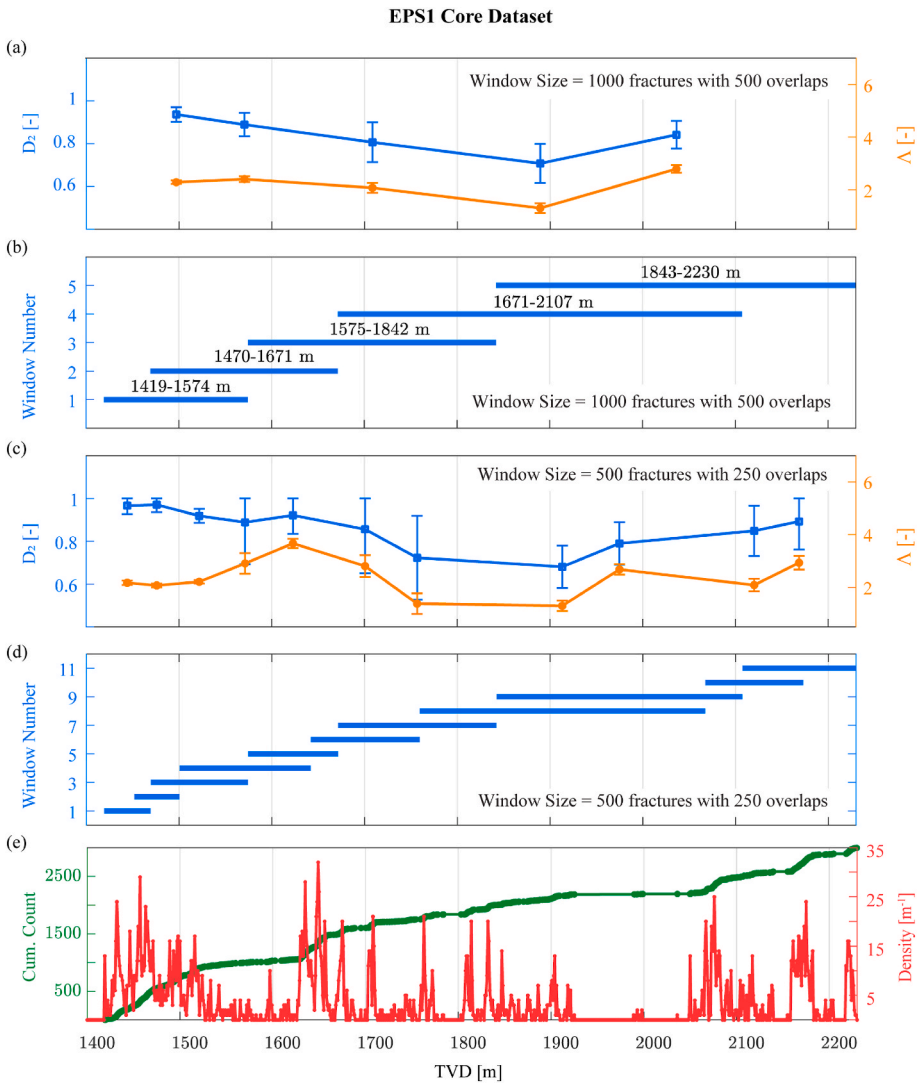


**Fig. 8.** (a) Estimates of $D_2$ (blue) and $\Lambda$ (orange) derived for sub-intervals containing 1000 fractures stepped along EPS1 with 500 fracture overlaps. The error estimates represent one standard deviation of the fits of the linear trends to the NCIs over the normalized range 0.001–0.1. The catchment depth range for each of the 1000-fracture intervals are shown below in (b). (c–d) Same as (a–b) but using 500-fracture intervals with 250 fracture overlaps. (e) Cumulative fracture count (green) and fracture density (red) along EPS1 from the core dataset. (For interpretation of the references to colour in this figure legend, the reader is referred to the Web version of this article.)

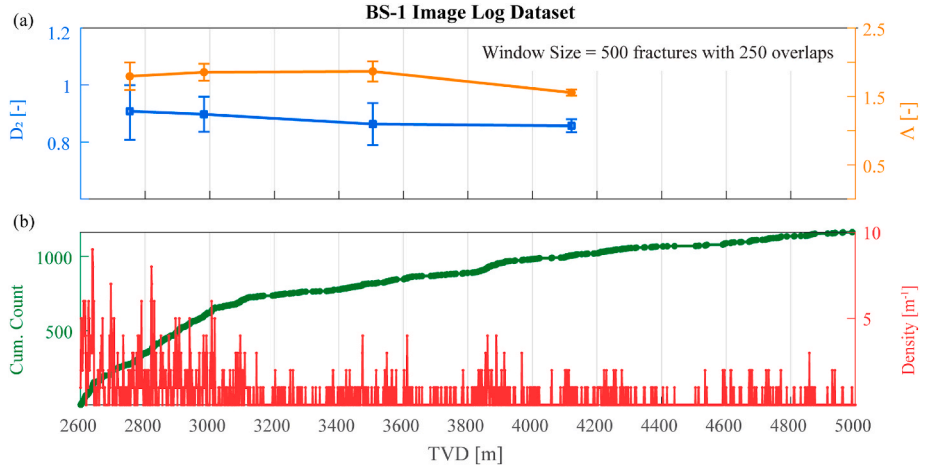


**Fig. 9.** (a) Variations of $D_2$ (blue) and $\Lambda$ (orange) versus depth in moving windows of 500 with 250 overlaps fractures along the BS-1 well. The vertical lines denote the errors of the $D_2$ and $\Lambda$ estimates. (b) Fracture frequency (green) and fracture density (red) along the BS-1 dataset. (For interpretation of the references to colour in this figure legend, the reader is referred to the Web version of this article.)

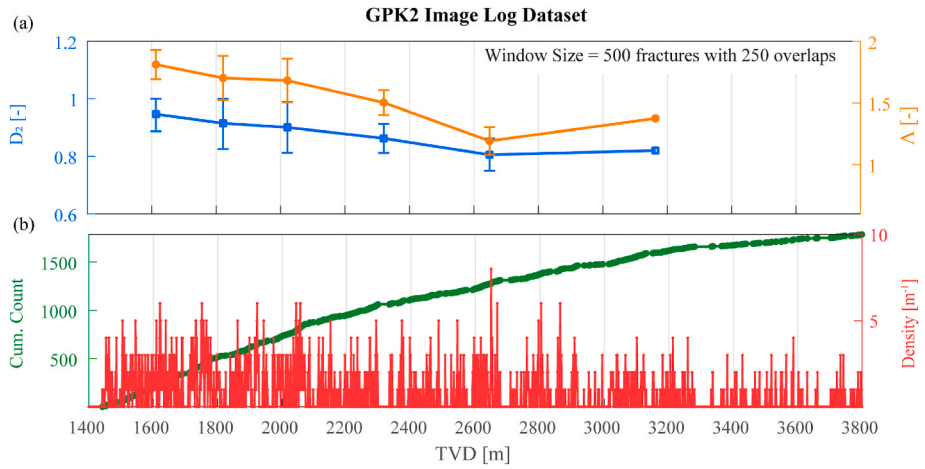


**Fig. 10.** (a) Variations of $D_2$ (blue) and $\Lambda$ (orange) versus depth in moving windows of 500 with 250 overlaps fractures along the GPK2 well. The vertical lines denote the errors of the $D_2$ and $\Lambda$ estimates. (b) Fracture frequency (green) and fracture density (red) along the GPK2 dataset. (For interpretation of the references to colour in this figure legend, the reader is referred to the Web version of this article.)

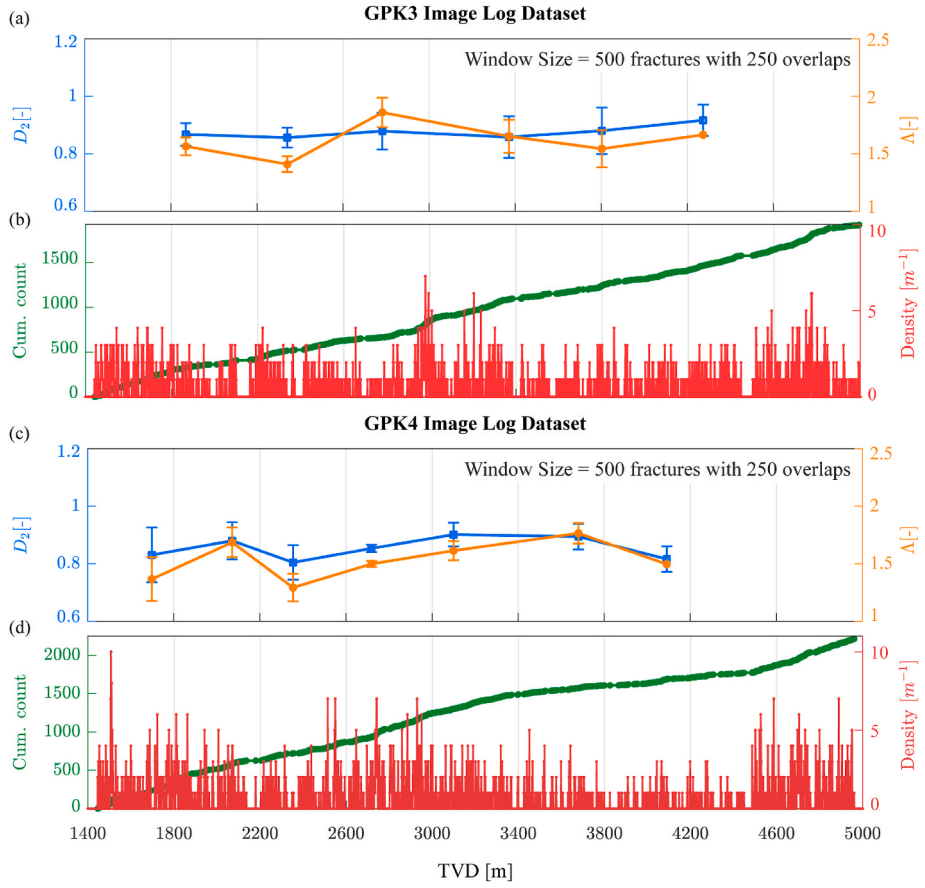


**Fig. 11.** (a,c) Variations of $D_2$ (blue) and $\Lambda$ (orange) versus depth in moving windows of 500 with 250 overlaps fractures along the GPK3-4 wells. The vertical lines denote the errors of the $D_2$ and $\Lambda$ estimates. (b,d) Fracture frequency (green) and fracture density (red) along the GPK3-4 datasets. (For interpretation of the references to colour in this figure legend, the reader is referred to the Web version of this article.)

($D_2$), power-law scaling coefficients ($\Lambda$), cumulative frequency, and fracture density versus depth plots of GPK2/3/4. The fracture densities in these datasets were more uniformly distributed compared to the BS-1 dataset. The mean values of $D_2$ varied between 0.81 and 0.94, and those for $\Lambda$ vary between 1.2 and 1.86. No systematic dependence of scaling laws to depth was observed along any of the boreholes.

## 5. Discussion

### 5.1. Fractal scaling of 1D fracture datasets

The correlation analyses of fractures in five image log datasets from deep crystalline basement rocks in the Upper Rhine Graben area demonstrated that the spatial distribution of fractures followed fractal

statistics. The correlation slope functions were relatively stable with little variation over at least two orders of magnitude in scale. The corresponding values of fractal dimension, $D_2$, and power-law scaling coefficient, $\Lambda$, varied between 0.85-0.90 and 1.49–2.3, respectively (Table 2). For the Soultz wells, this can be explained by a common geotectonic setting that controlled the fracture formation in similar lithologies during the geological history. In case of BS-1, the scaling exponent was also similar to the wells at Soultz in spite of being located in a distance of more than 150 km.

In contrast to the image log datasets, the correlation analyses applied to the full EPS1 core dataset yielded a relatively unstable slope function, the slope varying from 0.64 to 0.89 with a mean value of 0.8 over the range of approximate linearity of the NCI (Fig. 4a). The mean value is lower than the values found for the image log datasets (Table 2), and, taken on face value, would suggest a higher degree of fracture clustering than applies for the image log datasets, a result that is surprising given that EPS1 samples the same rock mass as the other four Soultz wells (Table 1). The core dataset differs from the others inasmuch as it affords a more complete sampling of fractures along the profile of the well. The image log datasets, particularly those from ultrasonic televiewers, rarely include fractures with apertures less than a few millimeters owing to their limited resolution. There are also sometimes difficulties in running logs in deep holes with breakouts or washouts, such as the Basel hole BS-1 where stick-slip movement of the sonde led to compromised fracture detections below 4.7 km.[32] To render the EPS1 core dataset more comparable to those from image logs, fractures with a width less than 1 mm were excluded and the scaling analysis repeated. The resulting normalized correlation integral (NCI) and slope functions shown in Fig. 4b are not significantly different to those obtained for the full dataset. Thus, it is unlikely that the resolution limit accounts for the difference in fractal dimension estimates obtained from the EPS1 core and the Soultz image logs.

### 5.2. Depth-dependent clustering and physical insight

A more probable explanation for the difference is suggested by the results of the depth-dependent analysis of the EPS1 core data shown in Fig. 8. The correlation dimension estimates obtained for 500- and 1000-fracture intervals whose fractures lie entirely above 1750 m or below 2070 m all have mean values between 0.85 and 1.0, and thus are consistent with the estimates from the image logs. In contrast, the estimates from intervals that include fractures located between 1750 m and 2070 m have significantly lower $D_2$ mean values, the lowest being 0.7 for the datapoints near 1900 m for both 500 and 1000-fracture profiles. The upper limits of the error bars for both these datapoints lie at or below 0.8, which is less than the lower limits of the errors obtained near the top of the EPS1 profiles, or those from the full-log analyses of the image log datasets (Table 2). Thus, we conclude that the difference in $D_2$ estimates obtained from the full EPS1 core and the Soultz image logs primarily reflects the presence of a localized zone between 1750 and 2070 m in EPS1 where the fractal fracture pattern is disturbed or takes a lower fractal dimension than elsewhere. A similar conclusion was reached by[45] who analyzed the EPS1 core dataset using a Cantor Dust method with 200 and 300 fracture windows with 100 fracture overlaps to obtain profiles of fractal dimension. Although their fractal dimension estimates were generally lower than ours, varying between 0.3 and 0.55 for the 300-fracture windows, they found a zone of low fractal dimension between 1800 and 2000 m, consistent with our observations (see their Fig. 5). That the interval in EPS1 between 1750 and 2070 is structurally unusual is indicated by the near-absence of fractures between 1920 and 2050 m, a 130 m hiatus that is not seen in any other well at the Soultz site. The near absence of fractures at the depth range 1920 and 2050 m has been noted by other authors (e.g. Ref. [53], but the reasons are unclear. One explanation is that it reflects the presence of structurally-controlled local stress shadows that developed during the geological history and which hindered the formation of fractures. Another factor may be that it reflects the presence of a petrologic fabric remnant from melt emplacement that was less favorable for fracture formation. Petrofabric measurements performed on primary minerals (biotite, quartz, plagioclase) in the EPS1 cores indicated that the magma flow during the emplacement of the granite was highly heterogeneous and that a fabric is present that varies along the hole.[78] It should be understood that although there are relatively few fractures in this 130 m sub-vertical profile, it does not imply that the same is true in horizontal directions.

[45] also reported a tendency for fractal dimension to increase with depth. Our analysis does not support this conclusion. Indeed, no systematic, statistically-significant depth-dependence of fractal dimension was resolved in any of the analyzed datasets. This applies to the well BS-1 at Basel, and the two Soultz wells GPK3/4 that sample the fracture population in the basement down to 5000 m, suggesting vertical homogeneity in fracture scaling to at least that depth at these sites (Figs. 9 and 11). Similarly, lateral homogeneity at scales of at least 1.5 km is suggested by the results from the five wells at the Soultz site (Fig. S2), although the lower fractal dimension obtained for the 1750–2070 m interval in EPS1 indicates that local anomalies can occur. In this regard, it is noteworthy that the higher fracture intensity observed in BS-1, which is associated with stress relaxation prior to Triassic times when the top of the crystalline basement at 2.5 km was at the surface, did not yield markedly different fractal dimension estimates to those obtained from deeper sections.

These results also showed that the 1D natural fracture datasets were stationary and hence the scaling relationships provided meaningful statistics of borehole datasets. A prerequisite for the stationarity is that the power-law scaling relationships do not vary upon translation and expansion/shrinkage.[33] Stationarity in translation of our results is implicitly demonstrated in the depth analysis of scaling where we found that scaling to be invariant with depth Moreover, our results conform to expansion/shrinkage stationarity because they were obtained with a normalized approach.

As noted earlier, the fractal dimension estimates for EPS1 obtained by[45]; which for the 300-fracture window ranged between 0.3 and 0.55 depending upon depth, were significantly lower than the values of 0.7–0.95 obtained here (Fig. 8). Such a discrepancy is probably related to the box-counting technique that is largely influenced by finite size effects. As stated earlier, this methodology is rather unstable, even when applied to synthetic fractal datasets.[40]

Each of the fracture datasets analyzed included the data from fracture zones that cut the well[23;79;80;50] These were not treated individually, but rather the collective data were considered as representative of a single fracture network. With the exception of the 1750–2070 m section of EPS1, essentially the same scaling was obtained for sub-intervals of the wells as the entire dataset, regardless of whether or not they contained fracture zones. In this vein, it is relevant to note that studies of scaling of single fracture zones have been reported that yield similar values of fractal dimension to those reported here.[74] analyzed the spatial distribution of cataclastic slip bands around damage zones of faults with various throws in sandstone outcrops. Band dataset was sampled along a 30 m fault-normal scanline at each site and found to display fractal scaling with correlation dimensions ranging between 0.85 and 0.91.[81] analyzed the clusters of fractures in shorter boreholes (between 10 and 50 m) intersecting two/three fault zones in crystalline rocks and reported correlation dimensions between 0.81 and 0.87. Collectively, these findings suggest that the spatial organization of fractures in 1D datasets follow relatively similar fractal scaling in different scales and geological settings.

The physical processes that control the scaling laws of fractures in fractured rock masses are not fully understood. One proposal is that the fractal dimension is related to the degree of fracture saturation in the rock during the formation of the network[40;38] Specifically, a more saturated system tends to have higher fractal dimension. In contrast to fractal dimension, relatively little attention has been paid to the multiplicative constant $\Lambda$ in the power-law scaling relation.[74] related $\Lambda$ to the

correlation length scale for damage around single faults, but this is not applicable to our analyses which features multiple fracture zones.[35] related $\Lambda$ to the fracture intensities over short scanlines of length <50 m. In Section 4.3, we evaluated this hypothesis over the longer intervals of relevance to the present study by generating 1D fracture pattern realizations over 1000 m length scales, each having the same fractal dimension and intensity. Although the $\Lambda$ values obtained from the NCI analysis of the realizations ranged between 1 and 2.25, which is similar to the values seen for natural fractures, no systematic dependence on intensity was obtained. Thus, $\Lambda$ is not simply related to fracture density, and other attributes of the network may be important. One possibility is that $\Lambda$ is related to lacunarity, the parameter that quantifies distribution of spaces between fracture patterns.[82] Understanding the potential linkage between $\Lambda$ and lacunarity or any other physical factor requires further investigations.

### 5.3. Implications

To conclude, it is worth emphasizing the importance of borehole fracture data for the construction of DFNs. In some deep earth-engineering projects, such as EGS development, the exploitation of oil and gas reservoirs, or the characterization of prospective $CO_2$ repositories, the only direct source of information about the fracture network within the rock mass of interest may stem from borehole logs. In such situations, the demonstration that the arrangement of fractures intersected along a borehole follows fractal statistics with a specific exponent would be an important step in building a DFN using a mathematical model such as the dual power-law model (Davy et al., 1990). This model is a versatile and efficient statistical representation of fractures that incorporates the spatial and length distribution of fractures in three dimensions. Parameterizing such DFN models at great depth, while challenging, can be accommodated by fractal analyses of 1D datasets from borehole data and the application of stereological relationships.[83] Although information on the 3D fracture length distribution cannot be obtained from borehole data alone, the assumption that it follows a power-law distribution (e.g. Ref. [84] allows DFNs to be generated with a length exponent that is allowed to vary over a reasonable range.

## 6. Conclusions

The analysis of the distribution of fractures in crystalline rocks imaged in five borehole logs up to 5 km deep from the Soultz and Basel EGS sites in the Rhine Graben showed that fracture arrangement followed fractal scaling laws at all scales upward of several meters that were amenable to assessment. Moreover, the fractal dimension in all cases was confined to the narrow range 0.85–0.9, despite the 150 km separation of the sites. A further fracture dataset which was derived from detailed analysis of 810 m of continuous core in granite to 2227 m at the Soultz site (i.e., well EPS1) showed significant deviation from fractal behavior. The mean fractal dimension of the best-fitted power-law was 0.8, which is less than the range 0.85–0.9 obtained from the analysis of logs in the neighboring wells. Exclusion of fractures with apertures less than 1 mm from the core dataset yielded even lower fractal dimension estimates, indicating that the limited resolution of imaging tools does not account for the difference in fractal dimension estimates of core and image datasets. Analysis of successive depth sections of the core log datasets showed the discrepancy was due to the presence of a localized zone between 1750 and 2070 m in the well where the fractal fracture pattern is disturbed or takes a lower fractal dimension than elsewhere. This zone is structurally unusual for the Soultz site inasmuch as it contains a 130 m interval that is almost free of natural fractures. No systematic change in fractal dimension with depth was observed in this or any other well. Indeed, depth section analyses applied to the five image log datasets yielded profiles of fractal dimension values that were consistent with those obtained from analysis of the full datasets. The results of this analyses will have significant implications for developing 3D DFN models of deep rock masses, especially in situations where borehole data provides the only direct sampling of the fracture population.

## Declaration of competing interest

The authors declare that they have no known competing financial interests or personal relationships that could have appeared to influence the work reported in this paper.

## Acknowledgements

This project has partially received funding from the European Union's Horizon 2020 research and innovation programme under grant agreement No 792037 (MEET project). The first author acknowledges support by the German Research Foundation (AF115/1-1).

## Appendix A. Supplementary data

Supplementary data to this article can be found online at https://doi.org/10.1016/j.ijrmms.2022.105138

## References

1 Ghassemi A. A review of some rock mechanics issues in geothermal reservoir development. *Geotech Geol Eng*. 2012;30:647–664. https://doi.org/10.1007/s10706-012-9508-3.
2 Iding M, Ringrose P. Evaluating the impact of fractures on the performance of the In Salah CO2 storage site. *Int J Greenh Gas Control*. 2010;4:242–248. https://doi.org/10.1016/j.egypro.2009.01.263.
3 Nelson R. *Geologic Analysis of Naturally Fractured Reservoirs*. Elsevier; 2001.
4 Reeves D, Parashar R, Zhang Y. Hydrogeologic characterization of fractured rock masses intended for disposal of radioactive waste, Radioactive Waste, Rehab Abdel Rahman. *IntechOpen*. 2012. https://doi.org/10.5772/33168.
5 Zoback MD, Kohli AH. *Unconventional Reservoir Geomechanics*. Cambridge University Press; 2019. https://doi.org/10.1017/9781316091869.
6 Frampton A, Hyman JD, Zou L. Advective transport in discrete fracture networks with connected and disconnected textures representing internal aperture variability. *Water Resour Res*. 2019;55:5487–5501. https://doi.org/10.1029/2018WR024322.
7 Nadimi S, Forbes B, Moore J, Podgorney R, McLennan JD. Utah FORGE: hydrogeothermal modeling of a granitic based discrete fracture network. *Geothermics*. 2020;87, 101853. https://doi.org/10.1016/j.geothermics.2020.101853.
8 Wu H, Fu P, Morris JP, et al. *Characterizing Fracture Flow in EGS Collab Experiment Based on Stochastic Modeling of Tracer Recovery, Workshop on Geothermal Reservoir Engineering*. California: Stanford; 2019.
9 Afshari Moein MJ. *Linkage between Fracture Network, Stress Heterogeneities and Induced Seismicity in Deep Geothermal Reservoirs*. Doctoral Dissertation. ETH Zurich; 2018.
10 Davy P, Darcel C, Le Goc R, Mas Ivars D. Elastic properties of fractured rock masses with frictional properties and power law fracture size distributions. *J Geophys Res Solid Earth*. 2018;123:6521–6539. https://doi.org/10.1029/2017JB015329.
11 Lavoine E, Davy P, Darcel C, Munier R. A discrete fracture network model With stress-driven nucleation: Impact on clustering, connectivity, and topology. *Front Phys*. 2020;8(9). https://doi.org/10.3389/fphy.2020.00009.
12 Lei Q, Wang X, Min K-B, Rutqvist J. Interactive roles of geometrical distribution and geomechanical deformation of fracture networks in fluid flow through fractured geological media. *J Rock Mech Geotech Eng*. 2020;12(4):780–792. https://doi.org/10.1016/j.jrmge.2019.12.014.
13 Fox DB, Koch DL, Tester JW. The effect of spatial aperture variations on the thermal performance of discretely fractured geothermal reservoirs. *Geotherm Energy*. 2015;3(2015):21. https://doi.org/10.1186/s40517-015-0039-z.
14 Gan Q, Elsworth D. Production optimization in fractured geothermal reservoirs by coupled discrete fracture network modeling. *Geothermics*. 2016;62:131–142. https://doi.org/10.1016/j.geothermics.2016.04.009.
15 Li S, Feng X-T, Zhang D, Tang H. Coupled thermo-hydro-mechanical analysis of stimulation and production for fractured geothermal reservoirs. *Appl Energy*. 2019;247:40–59. https://doi.org/10.1016/j.apenergy.2019.04.036.
16 Sun Z, Jiang C, Wang X, Lei Q, Jourde H. Joint influence of in-situ stress and fracture network geometry on heat transfer in fractured geothermal reservoirs. *Int J Heat Mass Tran*. 2020;149, 119216. https://doi.org/10.1016/j.ijheatmasstransfer.2019.119216.
17 Xin Y, Zhuang L, Sun Z. Numerical investigation on the effects of the fracture network pattern on the heat extraction capacity for dual horizontal wells in enhanced geothermal systems. *Geomech Geophys Geo-Energy Geo-Resour*. 2020;6(1):1–17. https://doi.org/10.1007/s40948-020-00151-3.
18 Yao C, Shao Y, , et alZhou C. Effects of fracture density, roughness, and percolation of fracture network on heat-flow coupling in hot rock masses with embedded three-

dimensional fracture network. *Geothermics*. 2020;87, 101846. https://doi.org/10.1016/j.geothermics.2020.101846.
19 Afshari Moein MJ, Somogyvári M, Valley B, Jalali M, Loew S, Bayer P. Fracture network characterization using stress-based tomography. *J Geophys Res Solid Earth*. 2018;123:9324–9340. https://doi.org/10.1029/2018JB016438.
20 Fadakar Alghalandis Y, Dowd PA, Xu C. The RANSAC method for generating fracture networks from micro-seismic event data. *Math Geosci*. 2013;45:207–224. https://doi.org/10.1007/s11004-012-9439-9.
21 Norbeck JH, Horne RN. Maximum magnitude of injection-induced earthquakes: a criterion to assess the influence of pressure migration along faults. *Tectonophysics*. 2018;733:108–118. https://doi.org/10.1016/j.tecto.2018.01.028.
22 Zhao Z, Illman WA. Three-dimensional imaging of aquifer and aquitard heterogeneity via transient hydraulic tomography at a highly heterogeneous field site. *J Hydrol*. 2018;559:392–410. https://doi.org/10.1016/j.jhydrol.2018.02.024.
23 Evans KF, Genter A, Sausse J. Permeability creation and damage due to massive fluid injections into granite at 3.5 km at Soultz: 1. Borehole observations. *J Geophys Res*. 2005;110, B04203. https://doi.org/10.1029/2004JB003168.
24 Schill E, Genter A, Cuenot N, Kohl T. Hydraulic performance history at the Soultz EGS reservoirs from stimulation and long-term circulation tests. *Geothermics*. 2017;70:110–124. https://doi.org/10.1016/j.geothermics.2017.06.003.
25 Amann F, Gischig V, alley B, et al. The seismo-hydromechanical behavior during deep geothermal reservoir stimulations: open questions tackled in a decameter-scale in situ stimulation experiment. *Solid Earth*. 2018;9:115–137. https://doi.org/10.5194/se-9-115-2018, 2018.
26 Ghergut J, Behrens H, Sauter M. Petrothermal and aquifer-based EGS in the Northern-German Sedimentary Basin, investigated by conservative tracers during single-well injection-flowback and production tests. *Geothermics*. 2016;63:225–241. https://doi.org/10.1016/j.geothermics.2016.01.015.
27 Pham HV, Parashar R, Sund N, Pohlmann K. Determination of fracture apertures via calibration of three-dimensional discrete-fracture-network models: application to Pahute Mesa, Nevada National Security Site, USA. *Hydrogeol J*. 2020:1–17. https://doi.org/10.1007/s10040-020-02254-3.
28 Wu H, Fu P, Morris JP, et al. Characterization of flow and transport in a fracture network at the EGS Collab field experiment through stochastic modeling of tracer recovery. *J Hydrol*. 2021;593, 125888. https://doi.org/10.1016/j.jhydrol.2020.125888.
29 Afshari Moein MJ, Tormann T, Valley B, Wiemer S. Maximum magnitude forecast in hydraulic stimulation based on clustering and size distribution of early microseismicity. *Geophys Res Lett*. 2018;45:6907–6917. https://doi.org/10.1029/2018GL077609.
30 Fan Z, Eichhubl P, Gale JFW. Geomechanical analysis of fluid injection and seismic fault slip for the Mw4.8 Timpson, Texas, earthquake sequence. *J Geophys Res Solid Earth*. 2016;121:2798–2812. https://doi.org/10.1002/2016JB012821.
31 Lu J, Ghassemi A. Estimating natural fracture orientations using geomechanics based stochastic analysis of microseismicity related to reservoir stimulation. *Geothermics*. 2019;79:129–139. https://doi.org/10.1016/j.geothermics.2019.01.003.
32 Ziegler M, Evans KF. Comparative study of Basel EGS reservoir faults inferred from analysis of microseismic cluster datasets with fracture zones obtained from well log analysis. *J Struct Geol*. 2020;130, 103923. https://doi.org/10.1016/j.jsg.2019.103923.
33 Bistacchi A, Mittempergher S, Martinelli M, Storti F. On a new robust workflow for the statistical and spatial analysis of fracture data collected with scanlines (or the importance of stationarity). *Solid Earth*. 2020;11(6):2535–2547. https://doi.org/10.5194/se-11-2535-2020, 2020.
34 Massiot C, Townend J, Nicol A, McNamara DD. Statistical methods of fracture characterization using acoustic borehole televiewer log interpretation. *J Geophys Res Solid Earth*. 2017;122(8):6836–6852. https://doi.org/10.1002/2017JB014115.
35 Sanderson DJ, Peacock DC. Line sampling of fracture swarms and corridors. *J Struct Geol*. 2019;122:27–37. https://doi.org/10.1016/j.jsg.2019.02.006.
36 Valley B. *The Relation between Natural Fracturing and Stress Heterogeneities in Deep-Seated Crystalline Rocks at Soultz-Sous-Forêts (France)*. Doctoral Dissertation. Zurich, Switzerland: ETH; 2007. https://doi.org/10.3929/ethz-a-005562794.
37 Bour O, Davy P, Darcel C, Odling N. A statistical scaling model for fracture network geometry, with validation on a multiscale mapping of a joint network (Hornelen Basin, Norway). *J Geophys Res*. 2002;107(B6). https://doi.org/10.1029/2001JB000176.
38 Davy P, Le Goc R, Darcel C, Bour O, de Dreuzy JR, Munier R. A likely universal model of fracture scaling and its consequence for crustal hydromechanics. *J Geophys Res*. 2010;115, B10411. https://doi.org/10.1029/2009JB007043.
39 Torabi A, Berg SS. Scaling of fault attributes: a review. *Mar Petrol Geol*. 2011;28(8):1444–1460. https://doi.org/10.1016/j.marpetgeo.2011.04.003.
40 Afshari Moein MJ, Valley B, Evans KF. Scaling of fracture patterns in three deep boreholes and Implications for constraining fractal discrete fracture network models. *Rock Mech Rock Eng*. 2019;52:1723–1743. https://doi.org/10.1007/s00603-019-1739-7.
41 Marrett R, Gale JFW, Gómez LA, Laubach SE. Correlation analysis of fracture arrangement in space. *J Struct Geol*. 2018;108:16–33. https://doi.org/10.1016/j.jsg.2017.06.012.
42 Gillespie P, Howard C, Walsh J, Watterson J. Measurement and characterisation of spatial distributions of fractures. *Tectonophysics*. 1993;226(1-4):113–141. https://doi.org/10.1016/0040-1951(93)90114-Y.
43 Merceron T, Velde B. Application of Cantor's method for fractal analysis of fractures in the Toyoha Mine, Hokkaido, Japan. *J Geophys Res Solid Earth*. 1991;96(B10):16641–16650. https://doi.org/10.1029/91JB01419.
44 Roy A, Perfect E, Dunne WM, McKay LD. Fractal characterization of fracture networks: an improved box-counting technique. *J Geophys Res Solid Earth*. 2007;112(B12). https://doi.org/10.1029/2006JB004582.
45 Ledésert B, Dubois J, Genter A, Meunier A. Fractal analysis of fractures applied to Soultz-sous-Forêts hot dry rock geothermal program. *J Volcanol Geoth Res*. 1993;57(1):1–17. https://doi.org/10.1016/0377-0273(93)90028-P.
46 Hentschel H, Procaccia I. The infinite number of generalized dimensions of fractals and strange attractors. *Phys Nonlinear Phenom*. 1983;8(3):435–444. https://doi.org/10.1016/0167-2789(83)90235-X.
47 Dèzes P, Schmid S, Ziegler P. Evolution of the European Cenozoic Rift system: interaction of the alpine and pyrenean orogens with their foreland lithosphere. *Tectonophysics*. 2004;389(1-2):1–33. https://doi.org/10.1016/j.tecto.2004.06.011.
48 Genter A, Traineau H. Analysis of macroscopic fractures in granite in the HDR geothermal well EPS-1, Soultz-sous-Forêts, France. *J Volcanol Geoth Res*. 1996;72(1-2):121–141. https://doi.org/10.1016/0377-0273(95)00070-4.
49 Voges A, Toloczyki M, Trurnit P, Wittekindt H. *Geologische Karte der BundesrepublikDeutschland 1:1.000.000*. Hannover: BGR; 1993.
50 Ziegler M, Valley B, Evans KF. Characterization of natural fractures and fracture zones of the Basel EGS reservoir inferred from geophysical logging of the Basel-1 well. In: *World Geothermal Congress Melbourne, Australia*. 2015:19–25.
51 Genter A, Traineau H, Dezayes C, Elsass P, Ledésert B. Fracture analysis and reservoir characterization of the granitic basement in the HRD Soultz project (France). *Geoth Sci Technol*. 1995;4(3):189–214.
52 Genter A, Castaing C, Dezayes C, Tenzer H, Traineau H, Villemin T. Comparative analysis of direct (core) and indirect (borehole imaging tools) collection of fracture data in the Hot Dry Rock Soultz reservoir (France). *J Geophys Res*. 1997;102(B7):15419–15431. https://doi.org/10.1029/97JB00626.
53 Genter A, Traineau H. Borehole EPS-1, Alsace, France: preliminary geological results from granite core analyses for Hot Dry Rock research. *Sci Drill*. 1992;3(5):205–214.
54 Tenzer H, Budeus P, Schellschmidt R. Fracture analyses in hot dry rock drillholes at Soultz and Urach by borehole televiewer measurements. In: *1992 Annual Meeting of the Geothermal Resources Council*. 1992:317–321.
55 Paillet F, Barton C, Luthi S, Rambow F, Zemanek J. Borehole imaging and its application in well logging-an overview. In: *Borehole Imaging*6001.
56 Häring MO, Schanz U, Ladner F, Dyer BC. Characterisation of the Basel 1 enhanced geothermal system. *Geothermics*. 2008;37(5):469–495. https://doi.org/10.1016/j.geothermics.2008.06.002.
57 Kaeser B, Kalt A, Borel J. *The crystalline basement drilled at the Basel-1 geothermal site, a preliminary petrologicalgeochemical study. Report to Geopower Basel AG for Swiss Deep Heat Mining Project Basel*. Switzerland: Institut de Géologie et d'Hydrogéologie, Université de Neuchâtel; 2007.
58 Valley, Evans KF. Stress orientation to 5 km depth in the basement below Basel (Switzerland) from borehole failure analysis. *Swiss J Geosci*. 2009;102(3):467–480. https://doi.org/10.1007/s00015-009-1335-z.
59 Genter A, Evans K, Cuenot N, Fritsch D, Sanjuan B. Contribution of the exploration of deep crystalline fractured reservoir of Soultz to the knowledge of enhanced geothermal systems (EGS). *Compt Rendus Geosci*. 2010;342(7):502–516. https://doi.org/10.1016/j.crte.2010.01.006.
60 Dezayes C, Genter A, Valley B. Structure of the low permeable naturally fractured geothermal reservoir at Soultz. *Compt Rendus Geosci*. 2010;342(7):517–530. https://doi.org/10.1016/j.crte.2009.10.002.
61 Sausse J, Dezayes C, Genter A, Bisset A. Characterization of fracture connectivity and fluid flow pathways derived from geological interpretation and 3D modelling of the deep seated EGS reservoir of Soultz (France). In: *Proceedings, Thirty-Third Workshop on Geothermal Reservoir Engineering, Stanford, California*. 2008.
62 Dezayes C, Genter A, Hooijkaas GR. Deep-seated geology and fracture system of the EGS Soultz reservoir (France) based on recent 5km depth boreholes. In: *Proceedings World Geothermal Congress, Antalya, Turkey*. 2005.
63 Genter A, Traineau H, Dezayes C, et al. Fracture analysis and reservoir characterization of the granitic basement in the HDR Soultz Project (France). *Int J Rock Mech Min Sci Geomech Abstracts*. 1996;33(2):69A, 69A, Elsevier Science.
64 Bonnet E, Bour O, Odling NE, et al. Scaling of fracture systems in geological media. *Rev Geophys*. 2001;39(3):347–383. https://doi.org/10.1029/1999RG000074.
65 Bhattacharya PM, Kayal J, Baruah S, Arefiev S. *Earthquake source zones in northeast India: seismic tomography, fractal dimension and b value mapping, Seismogenesis and Earthquake Forecasting: The Frank Evison*. vol. II. Springer; 2010:145–158. https://doi.org/10.1007/978-3-0346-0500-7_11.
66 Hirata T, Satoh T, Ito K. Fractal structure of spatial distribution of microfracturing in rock. *Geophys J Int*. 1987;90(2):369–374. https://doi.org/10.1111/j.1365-246X.1987.tb00732.x.
67 Kagan YY. Earthquake spatial distribution: the correlation dimension. *Geophys J Int*. 2007;168(3):1175–1194. https://doi.org/10.1111/j.1365-246X.2006.03251.x.
68 Nampally S, Padhy S, Dimri VP. Characterizing spatial heterogeneity based on the b-value and fractal analyses of the 2015 Nepal earthquake sequence. *Tectonophysics*. 2018;722:154–162. https://doi.org/10.1016/j.tecto.2017.11.004.
69 Tafti TA, Sahimi M, Aminzadeh F, Sammis CG. Use of microseismicity for determining the structure of the fracture network of large-scale porous media. *Phys Rev*. 2013;87(3), 032152. https://doi.org/10.1103/PhysRevE.87.032152.
70 Langenbruch C, Shapiro SA. Gutenberg-Richter relation originates from Coulomb stress fluctuations caused by elastic rock heterogeneity. *J Geophys Res Solid Earth*. 2014;119:1220–1234. https://doi.org/10.1002/2013JB010282.
71 Sahimi M, Tajer SE. Self-affine fractal distributions of the bulk density, elastic moduli, and seismic wave velocities of rock. *Phys Rev*. 2005;71(4), 046301. https://doi.org/10.1103/PhysRevE.71.046301.
72 Valley B, Evans K. *Preliminary Assessment of the Scaling Relationships of In-Situ Stress Orientation Variations Indicated by Wellbore Failure Data, Eurock 2014: Rock*

*Engineering and Rock Mechanics: Structures in and on Rock Masses*. Vigo, Spain: CRC Press; 2014:463–468.
73 Velde B, Dubois J, Moore D, Touchard G. Fractal patterns of fractures in granites. *Earth Planet Sci Lett*. 1991;104(1):25–35. https://doi.org/10.1016/0012-821X(91)90234-9.
74 Du Bernard X, Labaume P, Darcel C, Davy P, Bour O. Cataclastic slip band distribution in normal fault damage zones, Nubian sandstones, Suez rift. *J Geophys Res*. 2002;107(B7). https://doi.org/10.1029/2001JB000493.
75 Li JZ, Laubach SE, Gale JFW, Marrett RA. Quantifying opening-mode fracture spatial organization in horizontal wellbore image logs, core and outcrop: application to Upper Cretaceous Frontier Formation tight gas sandstones, USA. *J Struct Geol*. 2018;108:137–156. https://doi.org/10.1016/j.jsg.2017.07.005.
76 Wang Q, Laubach S, Gale J, Ramos M. Quantified fracture (joint) clustering in Archean basement, Wyoming: application of the normalized correlation count method. *Petrol Geosci*. 2019;25:415–428. https://doi.org/10.1144/petgeo2018-146.
77 Darcel C, Bour O, Davy P, de Dreuzy JR. Connectivity properties of two-dimensional fracture networks with stochastic fractal correlation. *Water Resour Res*. 2003;39:1272. https://doi.org/10.1029/2002WR001628cel.
78 Schulmann K, Jezek J, Venera Z. Perpendicular linear fabrics in granite: markers of combined simple shear and pure shear flows?. In: Bouchez JL, Hutton DHW, Stephens WE, eds. *Granite: From Segregation of Melt to Emplacement Fabrics. Petrology and Structural Geology*. vol. 8. Dordrecht: Springer; 1997. https://doi.org/10.1007/978-94-017-1717-5_10.
79 Haffen S, Geraud Y, Diraison M, Dezayes C. Determination of fluid-flow zones in a geothermal sandstone reservoir using thermal conductivity and temperature logs. *Geothermics*. 2013;46:32–41. https://doi.org/10.1016/j.geothermics.2012.11.001.
80 Sausse J, Dezayes C, Dorbath L, Genter A, Place J. 3D model of fracture zones at Soultz-sous-Forêts based on geological data, image logs, induced microseismicity and vertical seismic profiles. *Compt Rendus Geosci*. 2010;342:531–545. https://doi.org/10.1016/j.crte.2010.01.011.
81 Brixel B, Klepikova M, , et alLoew S. Tracking fluid flow in shallow crustal fault zones: 2. Insights from cross-hole forced flow experiments in damage zones. *J Geophys Res Solid Earth*. 2020;125. https://doi.org/10.1029/2019JB019108.
82 Roy A, Perfect E, Dunne WM, Odling N, Kim J-W. Lacunarity analysis of fracture networks: evidence for scale-dependent clustering. *J Struct Geol*. 2010;32(10):1444–1449. https://doi.org/10.1016/j.jsg.2010.08.010.
83 Darcel C, Bour O, Davy P. Stereological analysis of fractal fracture networks. *J Geophys Res*. 2003;108:2451. https://doi.org/10.1029/2002JB002091.
84 Scholz CH, Cowie PA. Determination of total strain from faulting using slip measurements. *Nature*. 1990;346:837–839.